HAL
open science

Giant negative thermal expansion across the first-order magnetoelastic transition in Hf0.86Ta0.14Fe2

L. V. B. Diop, O. Isnard, Mehdi Amara, F. Gay, J. P. Itié

To cite this version:

L. V. B. Diop, O. Isnard, Mehdi Amara, F. Gay, J. P. Itié. Giant negative thermal expansion across the first-order magnetoelastic transition in Hf0.86Ta0.14Fe2. Journal of Alloys and Compounds, 2020, 845, pp.156310. 10.1016/j.jallcom.2020.156310 . hal-02918967

HAL Id: hal-02918967

https://hal.science/hal-02918967v1

Submitted on 21 Aug 2020

HAL is a multi-disciplinary open access archive for the deposit and dissemination of scientific research documents, whether they are published or not. The documents may come from teaching and research institutions in France or abroad, or from public or private research centers.

L'archive ouverte pluridisciplinaire **HAL**, est destinée au dépôt et à la diffusion de documents scientifiques de niveau recherche, publiés ou non, émanant des établissements d'enseignement et de recherche français ou étrangers, des laboratoires publics ou privés.

Giant negative thermal expansion across the first-order magnetoelastic transition in $Hf_{0.86}Ta_{0.14}Fe_2$

L.V.B. Diop[1,2*], O. Isnard[2], M. Amara[2], F. Gay[2], J. P. Itié[3]

[1]Université de Lorraine, CNRS, IJL, F-54000 Nancy, France

[2]Univ. Grenoble Alpes, CNRS, Institut NEEL, BP166x, F-38042 Grenoble cedex 9, France

[3]Synchrotron SOLEIL, L'Orme Merisiers St Aubin BP48, F-91192 Gif Sur Yvette, France

ABSTRACT

With the use of neutron powder diffraction, we have discovered and characterized an extremely anisotropic thermal expansion, including negative thermal expansion (NTE), in an itinerant-electron system $Hf_{0.86}Ta_{0.14}Fe_2$. It is revealed that the intermetallic compound $Hf_{0.86}Ta_{0.14}Fe_2$ exhibits temperature-induced magnetic phase transitions from ferromagnetic (FM) to antiferromagnetic (AFM) order and then to the paramagnetic (PM) state upon heating. The FM-AFM transformation proceeds in a stepwise fashion, as a first-order phase transition, and is accompanied by an isomorphic (without change of symmetry) lattice collapse. The unit cell shrinks abruptly in the basal plane only, while it's dimension along the six-fold symmetry axis *c* changes continuously. The thermal evolution of the *a* lattice constant is found to drive the change from FM to AFM magnetic order. $Hf_{0.86}Ta_{0.14}Fe_2$ shows a 0.41 % spontaneous volume reduction across the FM-AFM first-order magnetic transition, where a giant NTE, with a crystallographic volume thermal expansion coefficient -164×10^{-6} K^{-1}, is observed. We further show that the AFM state can be transformed into a FM state by few-tesla magnetic fields, which results in a large positive magnetostriction. A remarkably large adiabatic temperature change of ΔT_{ad} = 2.2 K is obtained for a magnetic field change of 3 T around the FM-AFM transition temperature. Using angle dispersive synchrotron x-ray diffraction, the evolution of the lattice was investigated at room temperature under high pressures up to 25 GPa. The application of external pressure leads to the monotonous decrease of the unit-cell parameters. The contraction of the hexagonal lattice is anisotropic with a larger compression along the high-symmetry direction *c*. A bulk modulus of K_0 = 223 GPa has been determined from the pressure-volume relationship.

Keywords: Negative thermal expansion, Magnetoelastic transition, Magnetocaloric effect, Neutron powder diffraction, High pressure, Intermetallic compounds

* E-mail address: leopold.diop@univ-lorraine.fr

1. Introduction

Most solids expand when they are heated and shrink upon cooling (positive thermal expansion, PTE). However, although rare, some materials contract upon heating, featuring negative thermal expansion. Materials exhibiting the negative thermal expansion (NTE) properties are of great importance from the viewpoints of both fundamental research and technological applications [1-4]. NTE materials have enormous industrial merit because they can be used to tune and control the overall thermal expansion of materials. NTE materials are generally combined with PTE materials to fabricate the zero thermal expansion (ZTE) composites [5-11], which are desirable in many fields such as high-precision optics and aerospace [12-15]. NTE materials are mainly used as the thermal-expansion inhibitor for making the composites with precisely tailored coefficient of thermal expansion. Hence, there are a number of important potential applications of NTE materials used as, for example, high-precision optical mirrors, optical fiber reflective grating devices, athermalizer for Bragg grating, printed circuit boards and machinery parts.

Up to now materials of various kinds have been identified and studied for their potential as NTE materials. In addition to the well-known ZrW_2O_8 family of materials [4], NTE effects have also been reported in silicates β-$LiAlSiO_4$ [16], cyanides $Cd(CN)_2$ [17], ReO_3 [18], CuO nanoparticles [3], ScF_3 [19-21], $PbTiO_3$-based ferroelectrics [22], antiperovskite manganese nitrides [23, 24] and as well as reduced layered ruthenate $Ca_2RuO_{3.74}$ [25]. However, only a very limited number of NTE systems serve as high-performance thermal-expansion compensators, due to low coefficient of thermal expansion, the relatively narrow NTE temperature span, thermal expansion anisotropy, as well as low mechanical and/or electrical insulating properties. Traditional NTE materials with flexible framework in the crystal structure (e.g., ZrW_2O_8 and ScF_3) usually exhibit NTE over a temperature window as wide as 1000 K, but the related coefficient of linear thermal expansion, α, can hardly go beyond -10×10^{-6} K^{-1}. Unfortunately, their NTE coefficient, is so small that a large amount of addition is needed in order to obtain high-performance ZTE composites. Large coefficient of thermal expansion, which can efficiently compensate the thermal expansion of PTE matrix but with little influence on its original physical properties, is thus desirable for NTE material. To promote an even wider range of practical applications, it has been long desired to develop news materials with large NTE coefficient over a wide temperature window.

Large NTE has been discovered during the last decade in several classes of materials, particularly materials associated with a metal-insulator [25,26], intermetallic charge-transfer [27,28] or ferroelectric transition [29]. Recently, the utilization of a magnetic transition accompanied by large volume contraction upon heating is deemed as a promising avenue towards discovery of giant NTE. The effectiveness of this approach was recognized widely by the giant NTE observed on the Mn_3AN-based antiperovskite manganese nitrides [9,23,24,55,56,58] which use volume change due to the magnetic phase transition, i.e., magnetovolume effects. The giant NTE of the antiperovskite manganese nitrides strongly influenced subsequent research, leading to the discovery of many phase-transition-type NTE compounds such as $MnCo_{0.98}Cr_{0.02}Ge$ [30] and $La(Fe,Si,Co)_{13}$ [31], which display large magnetovolume effects. For instance, a large coefficient of linear thermal expansion $\alpha = -26\times10^{-6}$ K^{-1} was achieved in the itinerant-electron magnet $LaFe_{10.5}CoSi_{1.5}$ by proper chemical substitution in $La(Fe,Si)_{13}$-based alloys. In the magnetic materials, the magnetovolume effect may have a significant influence on the overall thermal expansion. A famous example is the Invar alloys [66,67], which exhibit very low PTE or NTE below the magnetic ordering Néel or Curie temperatures. The moment-volume instability was argued to cause NTE, which suppresses the usual PTE and consequently leads to the Invar effect. It is well known that the unit-cell volume of a ferromagnetic (FM) spin arrangement is usually larger than that of an antiferromagnetic (AFM) one; therefore NTE could be observed at the FM-AFM magnetic phase transition.

To this end, one interesting examples is the pseudo-binary system $Hf_{1-x}Ta_xFe_2$, when $0.1 < x < 0.3$. Laves phase compounds of $Hf_{1-x}Ta_xFe_2$ are itinerant-electron magnets. In the composition range $0.1 < x < 0.3$, the compounds show a first-order ferromagnetic (FM) to antiferromagnetic (AFM) phase transition upon heating [32-40]. This FM-AFM first-order magnetic phase transition is critical for applications, as it is accompanied by strong responses to relatively minor stimuli, such as large magnetocaloric [41-43], magnetoresistive [33,37] magnetostrictive [39,44] or pressure effects [33,44,45]. As a consequence of the extreme sensitivity of the FM-AFM transition temperature to external pressure, the stability domain of the ferromagnetic state of $Hf_{0.825}Ta_{0.175}Fe_2$ is significantly reduced under moderate pressure and the ferromagnetic ground state is even totally suppressed by hydrostatic pressure above 0.75 GPa (critical pressure) that corresponds to the decrease of volume of only 0.5% [33]. A detailed study of the interatomic Fe–Fe exchange coupling constants and their lattice dependence revealed that the ferromagnetic interaction with the first shell is dramatically

reduced upon contraction of the *a* cell parameter [46]. Another interesting result of the theoretical calculations reported in Ref. [46] is that the Fe6h–Fe6h coupling is always positive meaning that these interactions will favor a ferromagnetic arrangement within the atomic plane containing the Fe6h positions with Fe6h as near neighbors. The FM-AFM transition was shown to be accompanied by an extremely sharp decrease of the Fe2a–Fe6h exchange parameters for the first neighbors.

In the present work we investigate the magnetovolume effects in correlation with magnetic properties due to the Fe sublattice in the itinerant-electron system $Hf_{0.86}Ta_{0.14}Fe_2$, chosen in the most interesting part of the magnetic phase diagram with coexistence of ferromagnetic (FM) and antiferromagnetic (AFM) behavior. We report how first-order magnetic phase transition correlates to instabilities of magnetic structures in this intermetallic compound. To determine the spin arrangements and understand their coupling with the lattice, we conducted a detailed high-intensity neutron powder diffraction study as a function of temperature. Despite the extensive investigations noted above, there appears to have been no studies addressing the high-pressure behavior of the crystallographic sublattice in this series of compounds $(Hf,Ta)Fe_2$. To contribute to the understanding of the role of volume in the $(Hf,Ta)Fe_2$ system, we have investigated the external pressure effect (up to 25 GPa) on the structural properties of $Hf_{0.86}Ta_{0.14}Fe_2$ by means of high-resolution synchrotron x-ray diffraction. In the present study, the magnetization has been measured in the temperature range both below and above the magnetic ordering temperatures. The magnetovolume effects have also been evaluated by means of the magnetostriction measurements. Finally, in order to discuss the magnetocaloric properties of the $Hf_{0.86}Ta_{0.14}Fe_2$ compound, heat capacity, isothermal entropy change ΔS_M, and as well as adiabatic temperature change ΔT_{ad} have been investigated.

2. Experimental methods

Polycrystalline $Hf_{0.86}Ta_{0.14}Fe_2$ alloy was prepared by melting high purity starting elements (better than 99.95%) in a high frequency induction furnace under a purified atmosphere of argon. The sample was melted at least three times with the button flipped over after each melting, which is usually sufficient to achieve compositional homogeneity. The obtained ingot was wrapped in tantalum foil, sealed in an evacuated quartz tube, and subsequently annealed at 1273 K for one week. The room temperature crystal structure and

phase purity of the sample was analyzed using the x-ray powder diffraction pattern obtained at ambient pressure on a Siemens D5000 diffractometer with Co-Kα radiation.

Neutron powder diffraction (NPD) measurements were carried at the Institut Laue Langevin (ILL). About 3 g of $Hf_{0.86}Ta_{0.14}Fe_2$ powder were introduced into a cylindrical vanadium sample holder (D = 6 mm, H = 5 cm) and mounted on the stick of a He cryostat, whose contribution to the powder diffraction patterns was eliminated using a radial oscillating collimator. Several patterns were collected at selected temperatures ranging between 1.5 and 450 K on the high-intensity diffractometer D1B (λ = 2.52 Å and λ/2 = 1.26 Å) with a detector angular range coverage $5° \leq 2\theta \leq 128°$ which is especially suited for magnetic structure determination. All measurements were performed upon heating after temperature stabilization with typical acquisition times of 20 minutes per isotherm. A second set of powder diffraction patterns was collected while ramping temperature at 1 K/minute. All full-pattern magnetic and structural refinements of the diffraction data employed the FullProf Suite package [47] using the Rietveld method.

High-pressure synchrotron x-ray diffraction (SXRD) experiments were carried out at the PSICHÉ beamline (Synchrotron SOLEIL) at room temperature in angle-dispersive mode (λ = 0.37384 Å). Powder diffraction data under pressures of up to 25 GPa were obtained using diamond anvil cells. Steel gaskets were preindented and holes were drilled at the center of the indentation. Sample, along with ruby chips, were loaded at the center of the drilled cavity. The pressure-transmitting medium was a 4:1 methanol-ethanol mixture. Pressure was determined using the ruby fluorescence method [64]. In order to improve the powder statistic, the sample was rotated ±5° during the exposure. Two-dimensional diffraction images in the range $3° < 2\theta < 22°$ were recorded by means of a MAR detector and the resulting diffraction data were azimuthally integrated with the FIT2D program [48]. The unit-cell parameters were refined by a least-squares procedure using full diffraction profiles.

Magnetization curves were measured in static magnetic fields up to 10 T at temperatures ranging between 4 and 330 K as well as in fields up to 7 T at temperatures between 300 and 800 K using extraction-type magnetometers. A detailed description of the magnetometers can be found in Ref. [49]. Thermal expansion and magnetostriction were measured over a wide temperature range from 2.5 to 300 K in magnetic fields up to 6 T. The measurements were performed using a high accuracy capacitance dilatometer with a resolution better than 1 Å. The magnetic field is applied along a fixed horizontal direction, while the capacitance cell –together with the sample– can be rotated around the vertical axis.

Magnetostriction was measured, both parallel and perpendicular to the applied field. The heat capacity measurement in zero magnetic field was conducted by using a Physical Property Measurement System (PPMS of Quantum Design). The entropy change, ΔS_M, was calculated from magnetization isotherms by means of the Maxwell relation. The direct measurement of the adiabatic temperature change ΔT_{ad} was studied in temperature range around the magnetic transitions. The device constructed at Institut Néel CNRS was used. ΔT_{ad} was measured using a vacuum calorimeter with a superconducting coil that produces steady magnetic fields of up to 8 T. The measurements employed the extraction method.

3. Results and discussion

3.1. High-Pressure synchrotron x-ray diffraction (SXRD) study

Because of the observed intimate relation between the crystallographic structure and the magnetic behavior in this itinerant-electron compound, the application of an external hydrostatic pressure, thus changing the interatomic distances, should modify the transition temperatures, stabilizing the low-volume antiferromagnetic phase. To probe the pressure dependence of the crystal structure, angle dispersive synchrotron x-ray diffraction experiments have been performed up to 25 GPa at room temperature. A Rietveld refinement of the diffraction pattern recorded at ambient pressure is shown in Fig. 1, confirming that the compound crystallize in the hexagonal C-14 Laves phase structure type (space group $P6_3/mmc$). The corresponding crystal structure is depicted in Fig. 2. In such a crystal arrangement, the Hf/Ta atoms occupy the 4*f* (1/3, 2/3, *z*) Wyckoff position and the Fe atoms are located on two crystallographically inequivalent sites 2*a* (0, 0, 0) and 6*h* (*x*, 2*x*, 1/4). The unit cell contains 4 formula units and this crystal structure is typical of Frank and Kasper type intermetallic phases featured by icosahedral polyhedron with low coordination of 12 [65]. The Fe(2*a*) atoms have an axial symmetry (-3m) and a local environment which is made of 12 near neighbours: 6 of which are Hf/Ta ones and 6 Fe(6*h*) type. The Fe atoms at 6*h* position are forming layers of triangular net in plane perpendicular to the [110] crystallographic axis. These layers are stacked in such a way that they are leading to pentagonal antiprisms containing the other Fe(2*a*) sites. Despite its different local environment symmetry, the Fe(6*h*) position is also surrounded by 12 near neighbours: 2 Fe(2*a*) neighbours, 4 Fe located at 6*h*

and 6 Hf/Ta atoms. The local environment of Hf/Ta atoms consists of 3 Fe(2*a*) neighbours, 9 Fe(6*h*) neighbours, and 4 Hf/Ta neighbours.

Selected diffraction patterns during compression of the sample are compared in Fig.3. X-ray powder diffraction patterns collected at various fixed pressures show that the hexagonal symmetry of the atomic arrangement remains unaltered within the investigated compression range; no indication of a structural phase transition was found up to the highest applied pressure. In spite of the broadening of the Bragg peaks the diffraction patterns remain qualitatively the same than the one at ambient pressure. All the Bragg peaks could be identified to arise from the original C-14 Laves phase structure (space group $P6_3/mmc$). The Bragg peaks shift to larger angles due to the shrinkage of the lattice. Least-squares refinements based on full diffraction profiles reveal a linear decrease of the lattice parameters (*a* and *c*) upon compression (see Fig.4). The lattice constants decrease continuously with pressure, and values of da/dP = -6.85 10^{-3} Å GPa^{-1} and dc/dP = -11.06 10^{-3} Å GPa^{-1} are obtained. The contraction of the hexagonal lattice is anisotropic and more pronounced along the six-fold symmetry axis *c*. As seen from the crystallographic structure (Fig. 2), the arrangements of bonds and atoms perpendicular to *c*-axis direction are dense, while, along *c*-axis direction the atoms arrange loosely, which indicates it has considerable relaxation space on compression. The pressure dependence of the unit-cell volume is shown in Fig.5. The data were fitted to a third-order Birch-Murnaghan equation of state [59] where K_0' was fixed at 4. The performed fit results in V_0 = 171.82 $Å^3$ for the zero-pressure cell volume and K_0 = 223 GPa for the bulk modulus. The bulk modulus of $Hf_{0.86}Ta_{0.14}Fe_2$ is 1.1 times larger than that of the isostructural compound $TiFe_2$ (K_0 = 201 GPa) [60].

3.2. Neutron powder diffraction (NPD) study

The observation of multiple magnetic phase transitions in $Hf_{0.86}Ta_{0.14}Fe_2$ by macroscopic magnetic measurements urged us to perform NPD studies to establish the magnetic structures of this material and it's temperature dependence. A detailed Rietveld analysis has been performed on diffraction spectra collected at selected temperatures in order to refine the crystal structure and magnetic ordering. Representative patterns of the Rietveld refinements are shown in Figs.6a-6c. A summary of the crystallographic parameters and the Fe magnetic moments obtained from the fits at 350, 290 and 1.5 K are listed in Table I. The diffraction pattern measured at 350 K (paramagnetic state PM) is characteristic of the nuclear

Bragg scattering and it has been fitted to the *P6₃/mmc* $MgZn_2$-type phase found at room temperature.

The NPD pattern obtained at 1.5 K does not show any additional reflections as compared to the pattern recorded in the PM regime. $Hf_{0.86}Ta_{0.14}Fe_2$ exhibits a ferromagnetic (FM) ordering of Fe moments below 275 K. This FM structure only modifies intensities of the nuclear peaks and magnetic scattering was found on several lines such as (100), (101) and (002). The Fe magnetic moments have been refined independently for the two sites and lie within the basal plane of the hexagonal lattice. The corresponding FM spin configuration is illustrated in Fig.7a. At 1.5 K, the deduced magnetic moments of Fe at the 2*a* and 6*h* crystallographic positions are about 1.39 and 1.43 μ_B respectively. They are converted to 2.84 μ_B for one chemical formula, very consistent with the value of 2.86 μ_B obtained from the spontaneous magnetization of $Hf_{0.86}Ta_{0.14}Fe_2$ at 4 K. In order to confirm the refinement results Rietveld analysis has also been performed on the difference between the diffractogram collected at 1.5 and 350 K, the mean Fe magnetic moment ≈ 1.4 μ_B is found to be compatible (within the experimental error bars) to that listed above. The magnetic reliability factor corresponding to the fit of the difference pattern is slightly improved to R_{Mag} = 8.1%.

$Hf_{0.86}Ta_{0.14}Fe_2$ is antiferromagnetic (AFM) only in a limited temperature range between $T_{FM\text{-}AFM}$ = 275 K and T_N = 336 K. Over the same temperature region, the analysis of the position of the magnetic reflections indicates that the corresponding magnetic structure is defined by the propagation vector **k** = (0, 0, 0) meaning that the magnetic unit cell coincides with the crystallographic one. The best refinement at 290 K is achieved for the magnetic arrangement in which Fe(6*h*) spins align ferromagnetically within the same layer while the coupling between successive Fe(6*h*) layers is antiferromagnetic. The refined magnetic moment for Fe(6*h*) atoms at 290 K is 0.35 μ_B. The AFM phase displays a magnetic structure (Fig.7b) with two independent Fe sublattices: only 3/4 of the Fe atoms are involved in the AFM configuration, namely those occupying 6*h* positions, while Fe atoms at 2*a* sites are not magnetically ordered. Since the 2*a* position is an inversion centre for the 6*h* sublattice, the molecular field acting upon the 2*a* site from the Fe(6*h*) magnetic moments is cancelled by symmetry in this AFM spin arrangement. Therefore, Fe(2*a*) atoms carry no ordered magnetic moment in AFM state. The magnetic structures of $Hf_{0.86}Ta_{0.14}Fe_2$ are similar to those established elsewhere for neighbouring $Hf_{0.825}Ta_{0.175}Fe_2$ composition [40].

In Ref [35], Li *et al.*, claimed identifying very weak magnetic contribution associated with (111) peak and therefore considered frustrated AFM structures (q = 0 kagome AFM),

where magnetic moments of Fe at the 6*h* sites form the 120° structure in the basal plane and interlayer coupling can be either FM or AFM. However, the (111) peak (which is not crystallographically allowed in the $P6_3/mmc$ space group) is not present in our high-intensity diffraction patterns in spite of an excellent signal to noise ratio. In fact, the (111) peak is not present in either the high-resolution diffraction pattern taken at ECHIDNA (OPAL reactor)[35] or previous NPD measurements [37,40].

The thermal dependencies of the lattice constants *a* and *c*, the *c/a* ratio, and the unit-cell volume *V* are displayed in Fig.8a, 8b and 8c, respectively. At lower temperatures the lattice parameter *a* increases with an upward curvature as temperature increases, indicating a normal thermal expansion character in the FM state. At $T_{\text{FM-AFM}}$, *a* exhibits a large drop $\Delta a/a \approx 0.33$ % and the system transforms simultaneously to the AFM state. The *c* lattice parameter gradually increases upon heating across the entire investigated temperature interval 1.5 – 450 K. The first-order nature of the magnetic transition is reflected in the steep jump of the *a* lattice constant rather than the tiny change in *c* parameter. The *c/a* ratio and the unit-cell volume also display a discontinuity. The cell volume of the FM phase is larger than that of AFM phase, and the spontaneous volume magnetostriction accompanying the first-order magnetic transition is estimated to be about $\Delta V/V \approx 0.41$ %. This large magnetovolume effect is related to the amplitude difference of the Fe magnetic moment between the FM and AFM state. One can observe a peculiarly anisotropic character of the volume collapse at the magnetic phase transition: the lattice shrinks abruptly, but only in the basal plane. The dimension along the high-symmetry axis varies almost continuously across the transition. It can be seen that there exists a temperature region in which the unit-cell volume expands with decreasing temperature, i.e., NTE occurs. It suggests that the lattice expansion induced by the magnetic transition is larger than the thermal contraction due to the temperature decrease.

Based on the refined values of volume, we calculated the volumetric thermal expansion coefficient $\beta = (1/V)(\Delta V/\Delta T)$. The 0.41% volume contraction occurs over a temperature interval of $\Delta T \sim 25$ K. $\Delta V/V$ shows a prominent NTE effect between 270 K and 295 K and the corresponding volume thermal expansion coefficient is $\beta = -164\times10^{-6}$ K^{-1}. The NTE in $Hf_{0.86}Ta_{0.14}Fe_2$ compound is intimately linked to the width of the magnetoelastic FM-AFM phase transition. Our crystallographic volume thermal expansion coefficient is at least an order of magnitude larger than the value found in $(Hf,Nb)Fe_2$ [50,51] and $(Hf,Ti)Fe_2$ [52]. This value is on the same order of magnitude as the colossal negative thermal expansion

reported for fine-powdered $Mn_{0.98}CoGe$ (β = -423×10^{-6} K^{-1}) [53] and for $Bi_{0.95}La_{0.05}NiO_3$ (β = -413×10^{-6} K^{-1}) [27].

Magnetoelastic phase transitions, and more generally spontaneous magnetostriction effect, are a known source of negative thermal expansion [54], which has already been observed in various intermetallic materials, in particular $La(Fe,Co,Si)_{13}$ [31], Mn_3AN-based antiperovskite manganese nitrides [55,56], $(Hf,Ti)Fe_2$ [52] and $(Hf,Nb)Fe_2$ [50, 51]. In majority of these systems the NTE region is limited by the width of the magnetic transition which is usually narrow in bulk samples. This NTE temperature span can be enhanced by processing the material to broaden the transition, for instance by converting it into nanocrystalline form for applications [23,53,57,58]. The NTE properties can be tailored by the control of the microstructure scale.

3.3. Magnetic properties

Fig.9 presents the temperature dependence of the magnetization, *M(T)*, of zero-field-cooled (ZFC) sample measured upon heating in a 0.01 T magnetic field. The thermomagnetic curve of the thermally demagnetized $Hf_{0.86}Ta_{0.14}Fe_2$ sample displays a strong decrease at T_{FM-AFM} = 275 K due to the magnetic phase transition from the ferromagnetic to the antiferromagnetic state. The isofield magnetization curve shows a small peak at T_N = 336 K corresponding to the magnetic phase transition from an AFM state to a PM phase (inset of Fig.9). Upon heating, the magnetic state of $Hf_{0.86}Ta_{0.14}Fe_2$ intermetallic compound changes from the FM to the AFM, and then, to the PM state.

ZFC *M(T)* curves were also recorded in various applied magnetic fields in order to determine the extent of the shift in the transition temperature with external field. The shift of the FM-AFM transition temperature, [$\Delta T_{FM-AFM}(\mu_0 H) = T_{FM-AFM}(\mu_0 H) - T_{FM-AFM}(\mu_0 H=0)$], is plotted against magnetic field in Fig.10. The solid line is a linear fit to the observed values. It is clearly seen that the magnetic ordering temperature T_{FM-AFM} strongly increases with increasing external field at a rate of 6.3 K/T.

Isothermal magnetization, *M(H)*, has been measured at various temperatures. Only a selection of curves is shown in Fig.11 in order to preserve clarity of presentation. A typical ferromagnetic behavior is observed at temperatures below 275 K. Spontaneous magnetization M_S was determined as the ordinate of the crossing point of the linearly extrapolated low- and high-field portions of the *M(H)* curves. M_S amounts to 2.86 μ_B/f.u. at 4 K; leading to an

average magnetic moment of 1.43 μ_B per Fe atom. The spontaneous magnetization of our sample $Hf_{0.86}Ta_{0.14}Fe_2$ is consistent with 2.84 μ_B/f.u. and 2.91 μ_B/f.u. obtained for neighboring compositions like $Hf_{0.825}Ta_{0.175}Fe_2$ [33] and $Hf_{0.845}Ta_{0.155}Fe_2$ [61] respectively. Above 275 K, a salient feature of the magnetization isotherms is the presence of a field-induced metamagnetic phase transition between the AFM and FM states. The metamagnetic transition is rather broad in fields and the transition proceeds through a progressive conversion of the antiferromagnetic phase into ferromagnetic domains with increasing applied magnetic field.

3.4. Thermal expansion and Magnetostriction

In metal compounds, magnetovolume effects are strongly related to the magnetism. $Hf_{0.86}Ta_{0.14}Fe_2$ shows peculiar magnetic behaviors such as an itinerant-electron metamagnetic transition. Therefore, it is expected that $Hf_{0.86}Ta_{0.14}Fe_2$ compound exhibits large magnetostrictive effects. In order to get a deeper insight into the nature of the magnetic behavior (first-order character of the FM-AFM transition), macroscopic linear thermal expansion $\Delta L/L$ measurements have been performed on polycrystalline $Hf_{0.86}Ta_{0.14}Fe_2$ sample. The results within the temperature range 240 – 300 K are displayed in Fig.12. The FM-AFM first-order magnetic phase transition is accompanied with a significant change in the spontaneous (μ_0H = 0 T) linear thermal expansion. $\Delta L/L$ decreases upon heating (Fig.12); consequently, a negative thermal expansion (NTE) is observed from 240 K to 300 K, leading to the average linear thermal expansion coefficient $\alpha = (1/L)(\Delta L/\Delta T) = -17\times10^{-6}$ K^{-1} over a temperature range of 60 K. This value is about 2 times larger than that of the commercial NTE materials currently used, i.e., ZrW_2O_8 with $\alpha = -9\times10^{-6}$ K^{-1} [16]. Such a high NTE performance is also comparable to those of reported intermetallic NTE materials: in $Mn_3Ga_{0.7}Ge_{0.3}N_{0.88}C_{0.12}$, for example, $\alpha = -18\times10^{-6}$ K^{-1} [56] and in $LaFe_{10.5}CoSi_{1.5}$ $\alpha = -26\times10^{-6}$ K^{-1} [31].

To elucidate the magnitude of the volume change by the metamagnetic transition, we measured magnetostriction isotherms along the parallel ($\Delta L/L_{//}$) and perpendicular ($\Delta L/L\perp$) directions to the applied field. From these measurements, the anisotropic magnetostriction ($\Delta L/L_{//}$ - $\Delta L/L\perp$) and the forced volume magnetostriction ($\Delta V/V = \Delta L/L_{//} + 2\Delta L/L\perp$) were evaluated. The results of volume magnetostriction obtained at some selected temperatures are illustrated in Fig.13. In the AFM state (T > 275 K), the value of $\Delta V/V$ is small up to a critical

field $\mu_0 H_{cr}$ at which a rapid increase occurs as the sample undergoes a metamagnetic transition. In addition, when the applied field is brought back to zero, the system recovers the initial state. We observed a clear hysteresis against the field scan, which is characteristic of the first-order nature of the phase transition. The critical field for the metamagnetic transition and the width of the hysteresis decrease with increasing temperature. This is consistent with the magnetization behavior. On polycrystalline sample, the forced volume magnetostriction $\Delta V/V$ determined at 295 K and 6 T is as high as 0.27%.

The obtained value for the field-induced volume magnetostriction compares very well with the results from the spontaneous linear thermal expansion (Fig.12). It should be emphasized that the value of the forced volume magnetostriction is of the same order as the spontaneous volume change at $T_{FM\text{-}AFM}$, observed in the thermal variation of the unit-cell volume from neutron diffraction data (Fig.8c). This fact constitutes clear evidence that the effect of the magnetic field is to induce a transition from the low-volume AFM phase to the high-volume FM phase through a first-order magnetic phase transition at a certain critical field. Consequently, these results indeed demonstrate that the mechanism which produces the spontaneous effect can be triggered reversibly by the application of a magnetic field through a field-induced first-order transition at $\mu_0 H_{cr}$. The values of $\mu_0 H_{cr}$, determined from the peak position of the derivative of the volume magnetostriction isotherms, display a linear dependence with temperature in the range of our available magnetic fields (Fig.14). The above changes in volume are closely related to the intrinsic magnetic properties of the sample.

3.5. Magnetocaloric properties

The zero-magnetic-field heat capacity data are plotted as a function of temperature in Fig.15. The only noticeable anomaly of the curve, is a narrow peak at 277 K, in excellent agreement with the values obtained from NPD, dilatometric linear thermal expansion and the thermomagnetic curve measured upon heating. The sharpness of the heat capacity anomaly and its nonlambda shape give nevertheless further support to the first-order nature of the transition. To make an assessment of the magnetocaloric properties we calculated the magnetic entropy change ΔS_M. The entropy change was determined from the magnetization isotherms by numerical integration of one of the thermodynamic Maxwell's relations as described in Ref. [62]. The thermal dependence of ΔS_M in various magnetic field changes $\mu_0 \Delta H$ is illustrated in Fig.16. As expected, the magnitude of ΔS_M is large around $T_{FM\text{-}AFM}$. The

magnetic entropy change is negative across the FM to AFM transition region. The entropy peak strongly broadens asymmetrically toward high temperatures upon increasing the magnetic field, which is consistent with the first-order character of the phase transition. ΔS_M reaches a value of -1.45 J K^{-1} kg^{-1} under $\mu_0\Delta H$ = 1 T. For comparison purposes we note that, in a 1 T field ΔS_M is about -1.5 J K^{-1} kg^{-1} for $Hf_{0.83}Ta_{0.17}Fe_2$ [41]. Finally, we turn to the measurements of the adiabatic temperature change ΔT_{ad} for a direct determination of the magnetocaloric effect. The results are presented as ΔT_{ad} *vs* T in Fig.17. The maximum ΔT_{ad} amounts to 2.2 K for a magnetic field change of $\mu_0\Delta H$ = 3 T. Our value compare well with those found in the literature for isostructural compounds, ΔT_{ad} = 2 and 2.5 K for $Hf_{0.875}Ta_{0.125}Fe_2$ and $Hf_{0.825}Ta_{0.175}Fe_2$ respectively, under $\mu_0\Delta H$ = 3 T [42]. The values of ΔT_{ad} for $Hf_{1-x}Ta_xFe_2$ materials are low in comparison with the benchmark system, elemental Gd, which is employed in most of magnetic refrigerator prototypes precisely because of its large ΔT_{ad} ($\Delta T_{ad} \approx 7.5$ K for $\mu_0\Delta H$ = 3 T [63]).

4. Conclusions

Coupled microscopic and macroscopic experimental studies explained the underlying phenomena responsible for the giant NTE observed over a 25 K temperature range – volumetric thermal expansion coefficient -164×10^{-6} K^{-1}. It is revealed that this unusually large NTE is induced by the magnetic phase transition from FM to AFM states. Truly interesting is how this FM-AFM transition happens: it is of first order and is accompanied by a stepwise drop of the magnetic moment and by an isomorphic lattice collapse of a peculiar anisotropic kind. The unit cell shrinks abruptly, but only in the basal plane; its dimension along the *c*-axis varies continuously. Our study unambiguously demonstrates that the disappearance of the magnetic moment of the Fe atoms at the 2a site plays a crucial role in the NTE of this system and sheds light on searching for NTE materials by tuning the competing magnetic orders. We showed the influence of the magnetovolume effects on the magnetic phase stability. The magnetic phase transition between the AFM and FM states can be induced reversibly by the application of an external magnetic field, producing large magnetoelastic effects and making this material attractive also from the point of view of its potential applications for magnetostrictive transducers. At room temperature, the application of external pressure induces an anisotropic contraction of the unit cell with a larger compression along the *c* direction.

Acknowledgments

The authors gratefully acknowledge the Institut Laue Langevin for access to the neutron facility. We also acknowledge the French Synchrotron facility SOLEIL for the allocation of beam time (Proposal No. 20130584).

References

[1] A.D. Fortes, E. Suard, K.S. Knight, Science **331**, 742 (2011).
[2] Y.W. Long, N. Hayashi, T. Saito,M. Azuma, S. Muranaka, Y. Shimakawa, Nature **458**, 60 (2009).
[3] X.G. Zheng, H. Kubozono, H. Yamada, K. Kato, Y. Ishiwata, C.N. Xu, Nature Nanotechnol. **3**, 724 (2008).
[4] T.A. Mary, J.S.O. Evans, T. Vogt, A.W. Sleight, Science **272**, 90 (1996).
[5] J. Chen, X.R. Xing, C. Sun, P.G. Hu, R.B. Yu, X.W. Wang, L.H. Li, J. Am. Chem. Soc. **130**, 1144 (2008).
[6] I. Yanase, M. Miyagi, H. Kobayashi, J. Eur. Ceram. Soc. **29**, 3129 (2009).
[7] K. Takenaka, M. Ichigo, Compos. Sci. Technol. **104**, 47 (2014).
[8] R.J. Huang, Z. Chen, X.X. Chu, Z.X. Wu, L.F. Li, J. Compos. Mater. **45**, 1675 (2011).
[9] K. Takenaka, Sci. Technol. Adv. Mater. **13**, 013001 (2012).
[10] L. M. Sullivan and C. M. Lukehart, Chem. Mater. **17**, 2136 (2005).
[11] K. Takenaka, T. Hamada, D. Kasugai, N. Sugimoto, J. Appl. Phys. **112**, 083517 (2012).
[12] K. Kintaka, J. Nishii, Y. Kawamoto, A. Sakamoto, P. G. Kazansky, Opt. Lett. **27**, 1394 (2002).
[13] A. Sakamoto, T. Matano, H. Takeuchi, IEICE Trans. Electron. **E83C**, 1441 (2000).
[14] J. Chen, L. Hu, J. X. Deng, X.R. Xing, Chem. Soc. Rev. **44**, 3522 (2015).
[15] C.P. Romao, K.J. Miller, C.A. Whitman, M.A. White, B.A. Marinkovic, *Negative Thermal Expansion (Thermomiotic) Materials* (Elsevier, Amsterdam, 2013).
[16] A.W. Sleight, Inorg. Chem. **37**, 2854 (1998).
[17] A.E. Phillips, A.L. Goodwin , G.J. Halder, P.D. Southon, C.J. Kepert, Angew. Chem. Int. Ed. **47**, 1396 (2008).
[18] T. Chatterji, T.C. Hansen, M. Brunelli, P.F. Henry, Appl. Phys. Lett. **94**, 241902 (2009).
[19] C.W. Li, X. Tang, J.A. Muñoz, J.B. Keith, S.J. Tracy, D.L. Abernathy, B. Fultz, Phys. Rev. Lett. **107**, 195504 (2011).
[20] B.K. Greve, K.L. Martin, P.L. Lee, P.J. Chupas, K.W. Chapman, A.P.Wilkinson, J. Am. Chem. Soc. **132**, 15496 (2010).
[21] J.P. Attfield, Nature **480**, 465 (2011).
[22] J. Chen, K. Nittala, J.S. Forrester, J.L. Jones, J. Deng, R. Yu, X. Xing, J. Am. Chem. Soc. **133**, 11114 (2011).
[23] X. Song, Z. Sun, Q. Huang, M. Rettenmayr, X. Liu, M. Seyring, G. Li, G. Rao, F. Yin, Adv. Mater. **23**, 4690 (2011)
[24] K. Takenaka, M. Ichigo, T. Hamada, A. Ozawa, T. Shibayama, T. Inagaki, K. Asano, Sci. Technol. Adv. Mater. **15**, 015009 (2014).
[25] K. Takenaka, Y. Okamoto, T Shinoda, N. Katayama, Y. Sakai, Nature Commun. **8**, 14102 (2017).
[26] M. Braden, G. André, S. Nakatsuji, Y. Maeno Phys. Rev. B **58**, 847 (1998).
[27] M. Azuma, W. Chen, H. Seki, M. Czapski, S. Olga, K. Oka, M. Mizumaki, T. Watanuki, N. Ishimatsu, N. Kawamura, S. Ishiwata, M.G. Tucker, Y. Shimakawa J.P. Attfield, Nature Commun. **2**, 347 (2011).
[28] I. Yamada, K. Tsuchida, K. Ohgushi, N. Hayashi, J. Kim, N. Tsuji, R. Takahashi, M. Matsushita, N. Nishiyama, T. Inoue, T. Irifune, K. Kato, M. Takata, M. Takano, Angew Chem. Int. Ed. **50**, 6579 (2011).
[29] J. Chen, X.R. Xing, G.R. Liu, J.H. Li, Y.T. Liu, Appl. Phys. Lett. **89**, 101914 (2006).
[30] Y.Y. Zhao, F.X. Hu, L.F. Bao, J. Wang, H. Wu, Q.Z. Huang, R.R. Wu, Y. Liu, F.R. Shen, H. Kuang, M. Zhang, W.L. Zuo, X.Q. Zheng, J.R. Sun, B.G. Shen, J. Am. Chem. Soc. **137**, 1746 (2015).

[31] R. Huang, Y. Liu, W. Fan, J. Tan, F. Xiao, L. Qian, L.Li, J. Am. Chem. Soc. **135**, 11469 (2013).
[32] Y. Nishihara, Y. Yamaguchi, J. Phys. Soc. Jpn. **52**, 3630 (1983).
[33] L.V.B. Diop, J. Kastil, O. Isnard, Z. Arnold, J. Kamarad, J. Appl. Phys. **116**, 163907 (2014).
[34] P. Bag, R. Rawat, P. Chaddah, P.D. Babu, V. Siruguri, Phys. Rev. B **93** 014416, (2016).
[35] B. Li, X.H. Luo, H. Wang, W.J. Ren, S. Yano, C.W. Wang, J.S. Gardner, K.D. Liss, P. Miao, S.H. Lee, T. Kamiyama, R.Q. Wu, Y. Kawakita, Z.D. Zhang, Phys. Rev. B **93**, 224405 (2016).
[36] L.F. Li, P. Tong, Y.M. Zou, W. Tong, W.B. Jiang, Y. Jiang, X.K. Zhang, J.C. Lin, M. Wang, C. Yang, X.B. Zhu, W.H. Song, Y.P. Sun, Acta Materialia **161**, 258 (2018).
[37] H.G.M. Duijn, E. Brück, A.A. Menovsky, K.H.J. Buschow, F.R. de Boer, R. Coehoorn, M. Winkelmann, K. Siemensmeyer, J. Appl. Phys. **81**, 4218 (1997)
[38] L. Li, P. Tong, W. Tong, W. Jiang, Y. Ding, H. Lin, J. Lin, C. Yang, F. Zhu, X. Zhang, X. Zhu, W. Song, Y. Sun, Inorg. Chem. **58**, 16818, (2019)
[39] L.V.B. Diop, M. Amara, O. Isnard, J. Phys.: Condens. Matter **25**, 416007 (2013).
[40] L.V.B. Diop, O. Isnard, E. Suard, D. Benea, Solid. State Commun. **229**, 16 (2016).
[41] J.F. Herbst, C.D. Furerst, R.D. McMichael, J. Appl. Phys. **79**, 5998 (1996).
[42] L.V.B. Diop, J. Kastil, O. Isnard, Z. Arnold, J. Kamarad, J. Alloys Compd. **627**, 446 (2015).
[43] Z.D. Han, D.H. Wang, S.L. Huang, Z.H. Su, S.L. Tang, Y.W. Du, J. Alloys Compd. **377**, 75 (2004).
[44] L. Morellon, P.A. Algarabel, M.R. Ibarra, Z. Arnold, J. Kamarad, J. Appl. Phys. **80**, 6911 (1996).
[45] L. V. B. Diop, Z. Arnold, O. Isnard, J. Magn. Magn. Mater. **395**, 251 (2015).
[46] L. V. B. Diop, D. Benea, S. Mankovsky, and O. Isnard, J. Alloys Compd. **643**, 239 (2015).
[47] J. Rodrıguez-Carvajal, Physica B **192**, 55 (1993).
[48] A.P. Hammersley, S.O. Svensson, M. Hanfland, A.N. Fitch, D. Hausermann, High Press. Res. **14**, 235 (1996).
[49] A. Barlet, J.C. Genna, P. Lethuillier, Cryogenic **31**, 801 (1991).
[50] H. Yibole, A.K. Pathak, Y. Mudryk, F. Guillou, N. Zarkevich, S. Gupta, V. Balema, V.K. Pecharsky, Acta Materialia **154**, 365 (2018).
[51] Y. Song, J. Chen, X. Liu, C. Wang, Q. Gao, Q. Li, L. Hu, J. Zhang, S. Zhang, X. Xing, Chem. Mater. **29**, 7078 (2017).
[52] Y. Qiao, Y. Song, K. Lin, X. Liu, A. Franz, Y. Ren, J. Deng, R. Huang, L. Li, J. Chen, X. Xing, Inorg. Chem. **58**, 5380 (2019).
[53] J. Lin, P. Tong, K. Zhang, H. Tong, X. Guo, C. Yang, Y. Wu, M. Wang, S. Lin, L. Chen, W. Song, Y. Sun, Appl. Phys. Lett. **109**, 241903 (2016).
[54] G.D. Barrera, J.A.O. Bruno, T.H.K. Barron, N.L. Allan, J. Phys.: Condens. Matter **17**, R217 (2005).
[55] T. Hamada, K. Takenaka J. Appl. Phys. **109**, 07E309 (2011).
[56] K. Takenaka, H. Takagi, Appl. Phys. Lett. **87**, 261902 (2005).
[57] Z. Sun, X. Song, J. Mater. Sci. Technol., **30**, 903 (2014).
[58] J.C. Lin, P. Tong, X.J. Zhou, H. Lin, Y.W. Ding, Y.X. Bai, L. Chen, X.G. Guo, C. Yang, B. Song, Y. Wu, S. Lin, W.H. Song, Y.P. Sun, Appl. Phys. Lett. **107**, 131902 (2015).
[59] F. Birch, Phys. Rev. **71**, 809 (1947).
[60] Y. Wu, X. Wu, S. Qin, K. Yang, J. Alloys Compd. **558**, 160 (2013).
[61] Y. Nagata, T. Hagii, S. Yashiro, H. Samata, S. Abe, J. Alloys Compd. **292**, 11 (1999).
[62] V.K. Pecharsky, K.A. Gschneidner Jr., J. Appl. Phys. **86**, 565 (1999).
[63] K.A. Gschneidner Jr., V.K. Pecharsky, A.O. Tsokol, Rep. Prog. Phys. **68**, 1479 (2005).
[64] H.-K. Mao, J. Xu and P. M. Bell, J. Geophys. Res. **91**, 4673 (1986).
[65] F. C. Frank and J. S. Kasper, Acta Crystallogr. **11**, 184 (1958).
[66] E.F. Wasserman, Invar: moment-volume instabilities in transition metals and alloys, in Ferromagnetic Materials, ed. by K.H.J. Buschow and E.P. Wohlfartht, Vol. 5 (Elsevier Science Publishers B.V., 1990), Chapter 3.
[67] E.F. Wasserman, J. Magn. Magn. Mater. **100**, 346 (1991).

	FM	AFM	PM
Temperature (K)	1.5	290	350
a (Å)	4.947(1)	4.934(2)	4.937(2)
c (Å)	8.061(2)	8.065(3)	8.074(2)
Hf /Ta (4f)			
z	0.063(1)	0.065(2)	0.066(1)
Fe (6h)			
x	0.832(3)	0.831(2)	0.831(1)
$y = 2x$	1.664(4)	1.662(4)	1.662(3)
Fe 2*a* moment (μ_B)	1.39(4)	—	—
Fe 6*h* moment (μ_B)	1.43(3)	0.35(8)	—
Moment—*c*-axis angle (°)	90	90	—
χ^2	4.92	4.12	5.02
R_{Bragg} (%)	7.11	5.83	4.57
R_{mag} (%)	8.30	13.3	—
R_{wp} (%)	10.6	11.3	8.20
R_p (%)	11.35	12.4	9.60
R_{exp} (%)	4.17	5.68	3.58

Table 1. Rietveld refinement results and reliability factors obtained from the analysis of the powder neutron diffraction patterns recorded at 1.5 K, 290 K and 350 K.

Figures

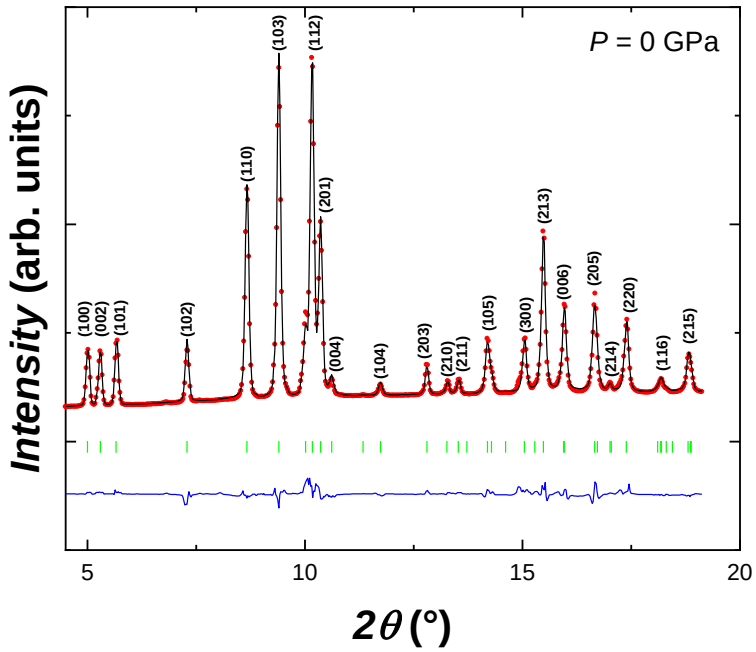

Fig. 1. Rietveld refinement of the synchrotron x-ray diffraction pattern of $Hf_{0.86}Ta_{0.14}Fe_2$ at ambient pressure (λ = 0.37384 Å).

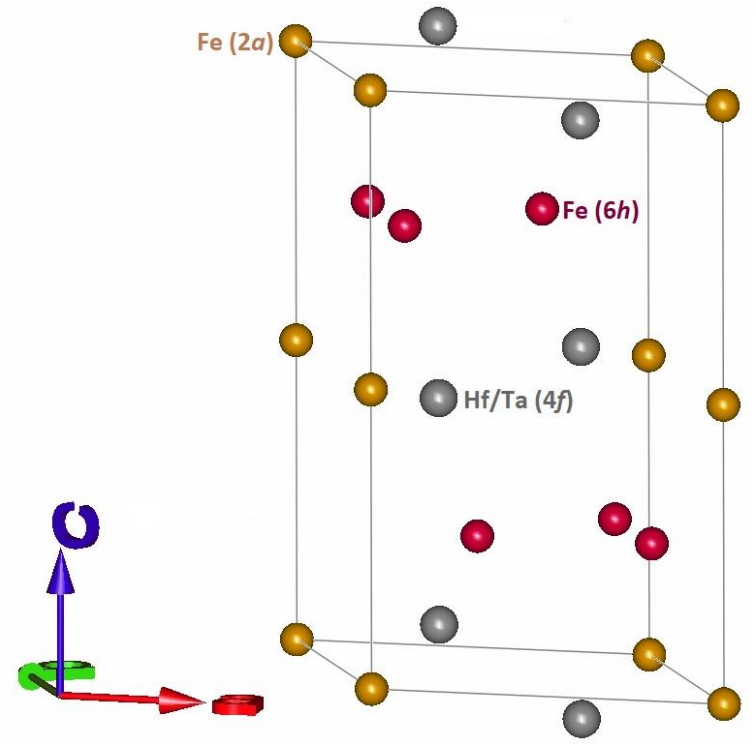

Fig. 2. Crystal structure of $Hf_{0.86}Ta_{0.14}Fe_2$.

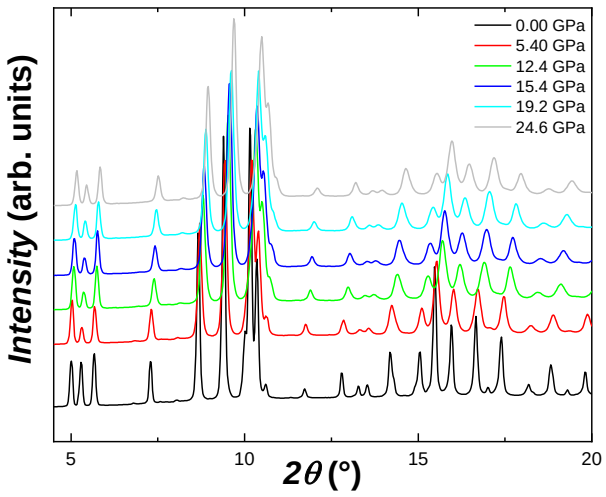

Fig. 3. Synchrotron x-ray diffraction patterns collected at room temperature for $Hf_{0.86}Ta_{0.14}Fe_2$ at various applied pressures (λ = 0.37384 Å).

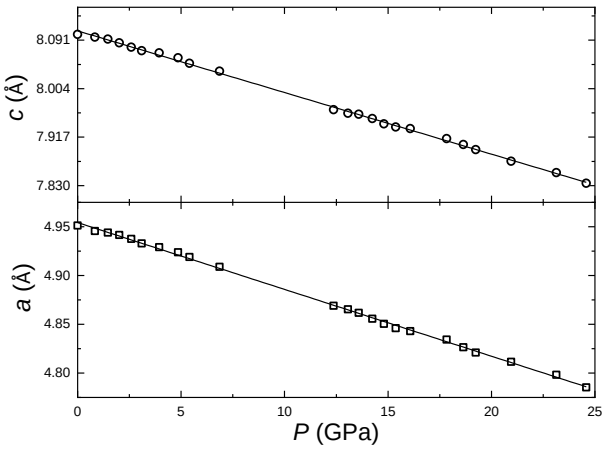

Fig. 4. Lattice parameters of $Hf_{0.86}Ta_{0.14}Fe_2$ as a function of applied pressure. The solid lines correspond to linear fits.

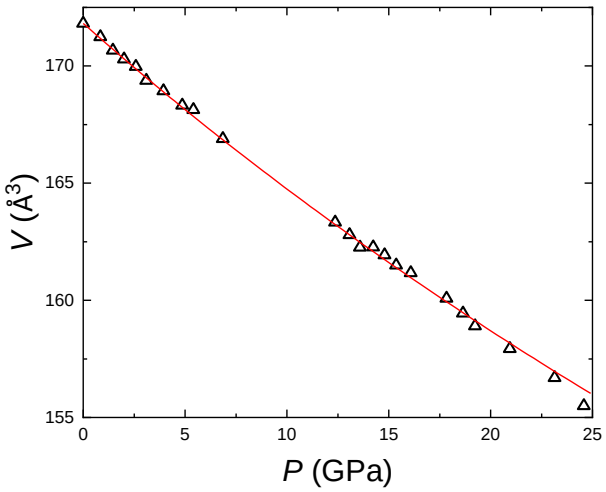

Fig. 5. Unit-cell volume of $Hf_{0.86}Ta_{0.14}Fe_2$ as a function of applied pressure. The continuous red line represents the third-order Birch-Murnaghan fit for the data.

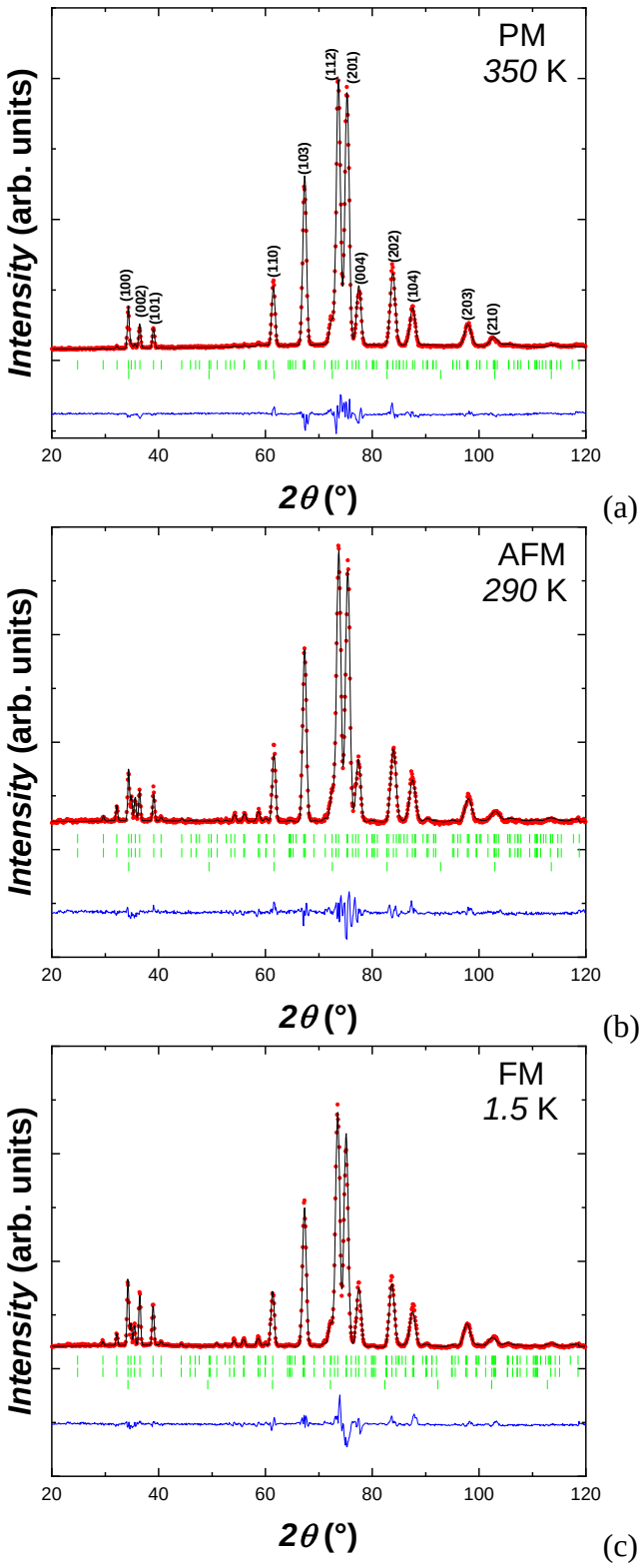

Fig. 6. Rietveld refinements of the neutron diffraction patterns for $Hf_{0.86}Ta_{0.14}Fe_2$ taken 350 K (a), 290 K (b) and 1.5 K (c). In the 350 K pattern, the top row of Bragg markers is for the $Hf_{0.86}Ta_{0.14}Fe_2$ nuclear contributions, the second row corresponds to the position of the sample environment and container made of vanadium. At 1.5 and 290 K the top and second rows of Bragg markers are referring to the nuclear and magnetic contributions of the $Hf_{0.86}Ta_{0.14}Fe_2$ phase. The third row is corresponding to the nuclear contribution from the vanadium sample environment.

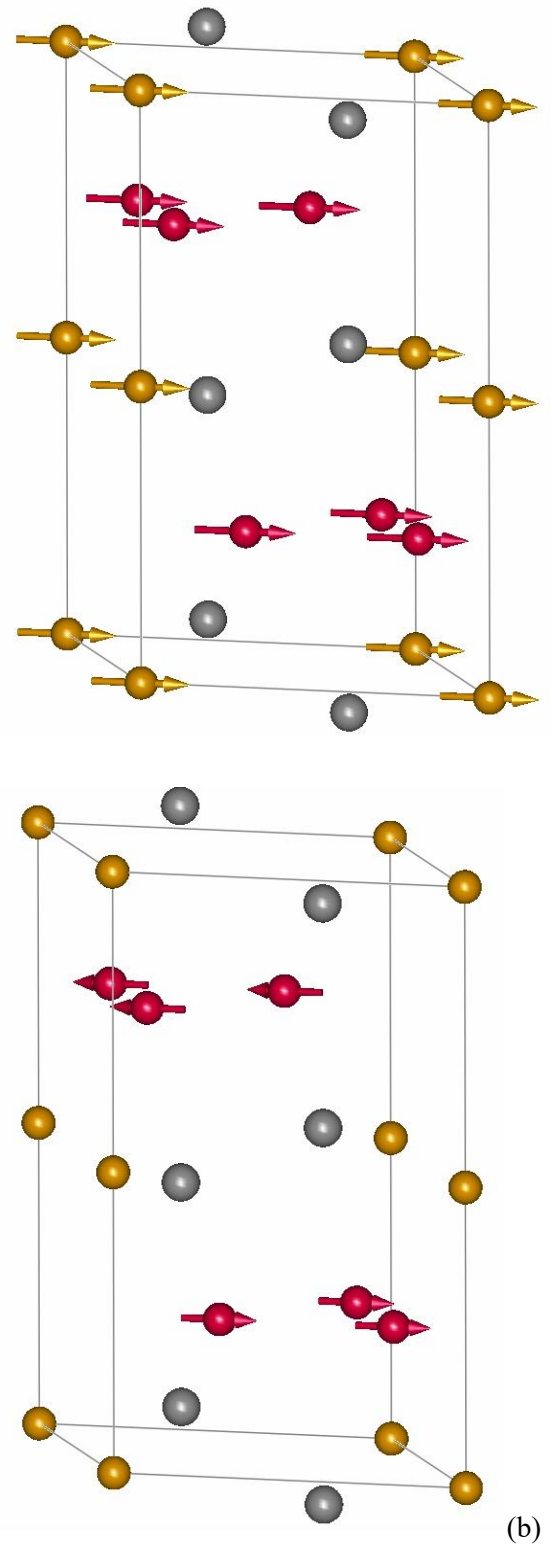

Fig. 7. Schematic representation of the magnetic structure of $Hf_{0.86}Ta_{0.14}Fe_2$ at 1.5 K (a) and 290 K (b).

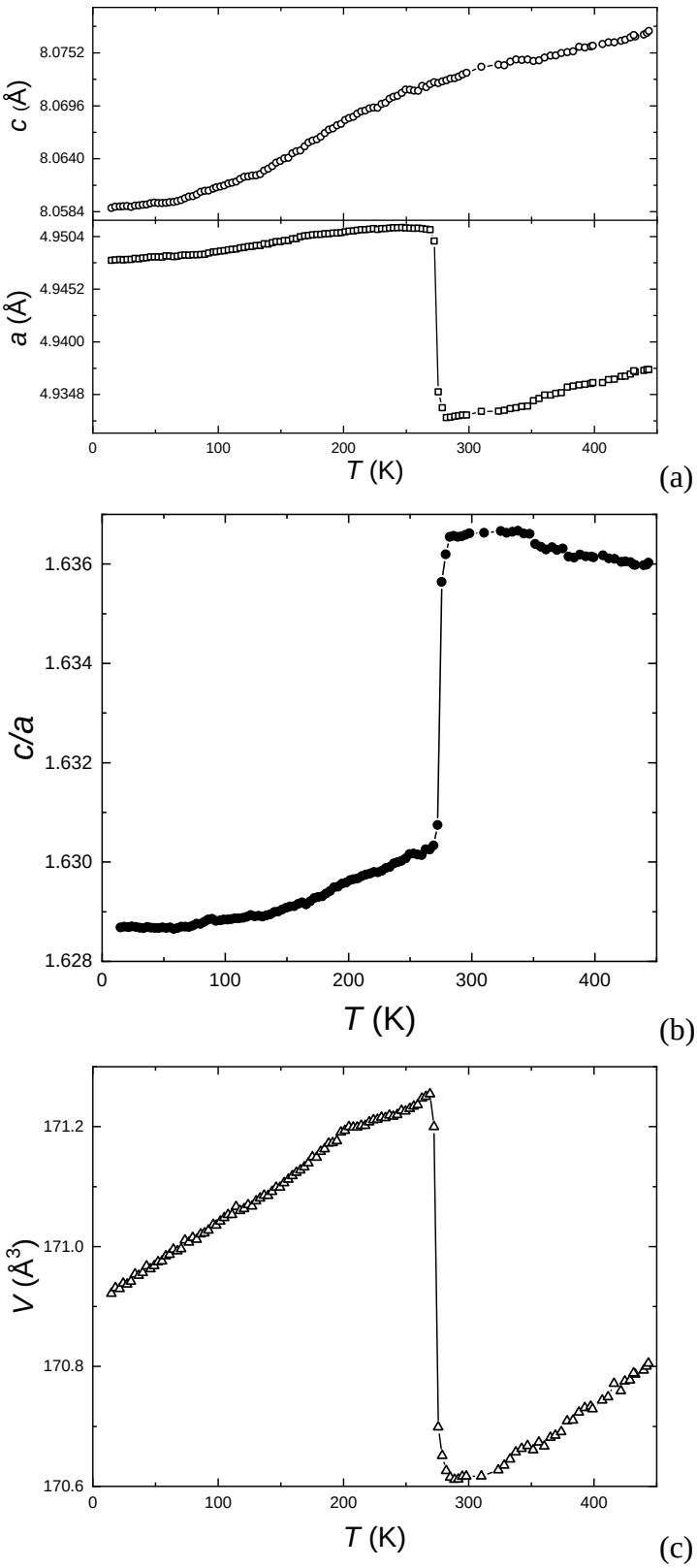

Fig. 8. Temperature dependence of the lattice parameters (a), *c/a* ratio (b), and unit-cell volume (c) obtained from Rietveld refinement of NPD data measured upon heating for $Hf_{0.86}Ta_{0.14}Fe_2$.

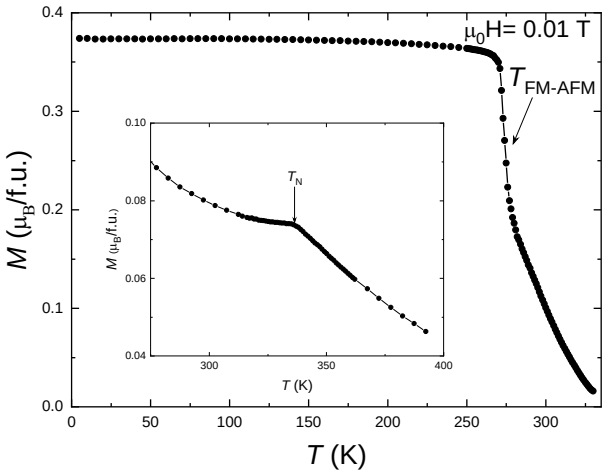

Fig. 9. Temperature dependence of the magnetization for $Hf_{0.86}Ta_{0.14}Fe_2$.

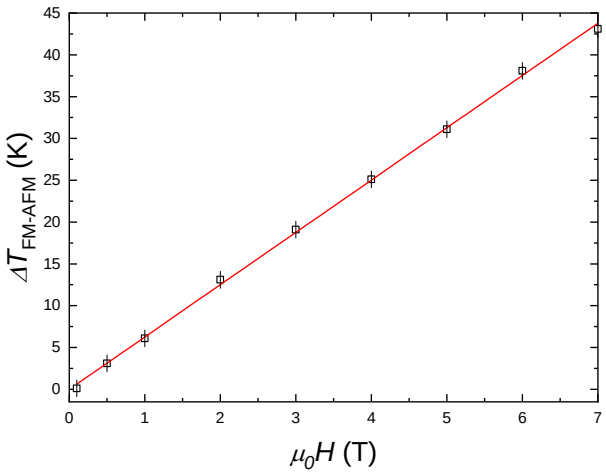

Fig. 10. Magnetic field dependence of the shift of the FM-AFM transition temperature $\Delta T_{\text{FM-AFM}}$ for $Hf_{0.86}Ta_{0.14}Fe_2$.

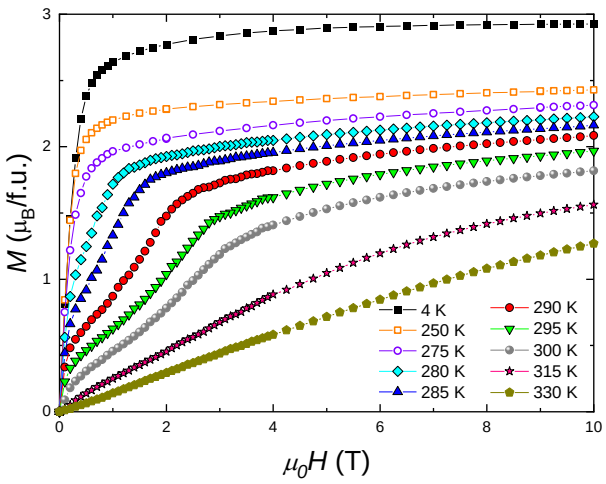

Fig. 11: Isothermal magnetization curves recorded at different temperatures for $Hf_{0.86}Ta_{0.14}Fe_2$.

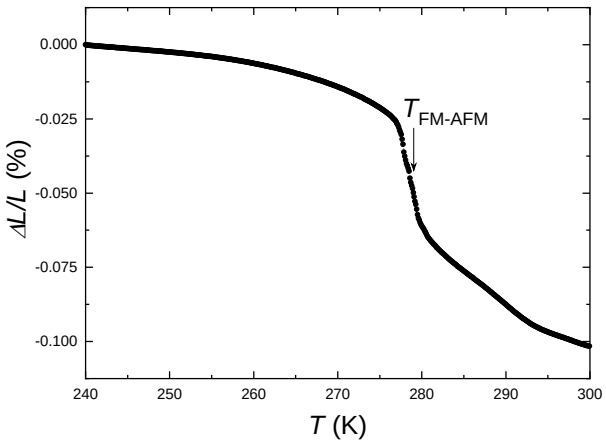

Fig. 12. Linear thermal expansion curve measured in zero applied field for $Hf_{0.86}Ta_{0.14}Fe_2$.

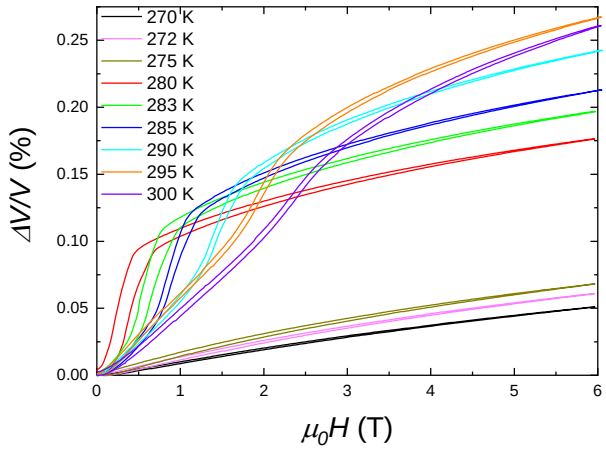

Fig. 13. Volume magnetostriction isotherms at some selected temperatures for $Hf_{0.86}Ta_{0.14}Fe_2$.

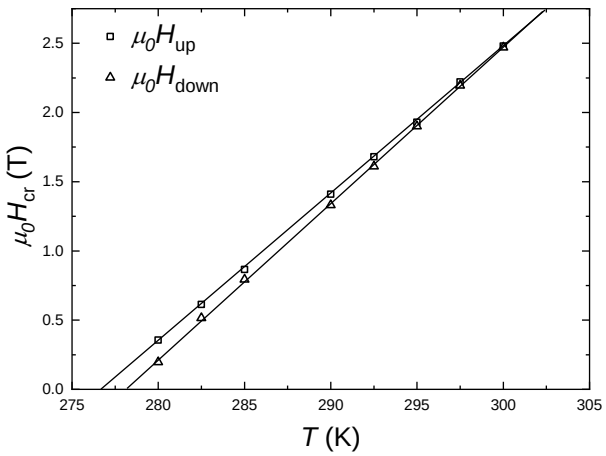

Fig. 14. Temperature dependence of the critical field $\mu_0 H_{cr}$ for $Hf_{0.86}Ta_{0.14}Fe_2$.

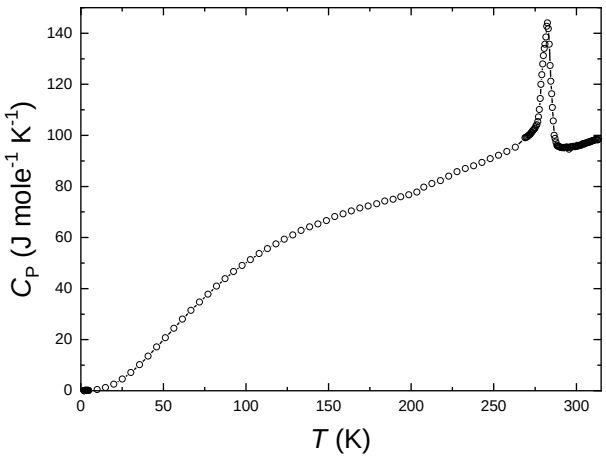

Fig. 15. Thermal variation of the heat capacity for $Hf_{0.86}Ta_{0.14}Fe_2$.

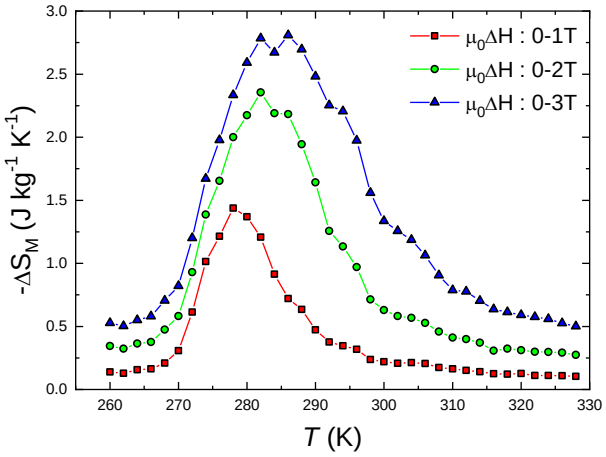

Fig. 16. Thermal variation of the magnetic entropy change for $Hf_{0.86}Ta_{0.14}Fe_2$.

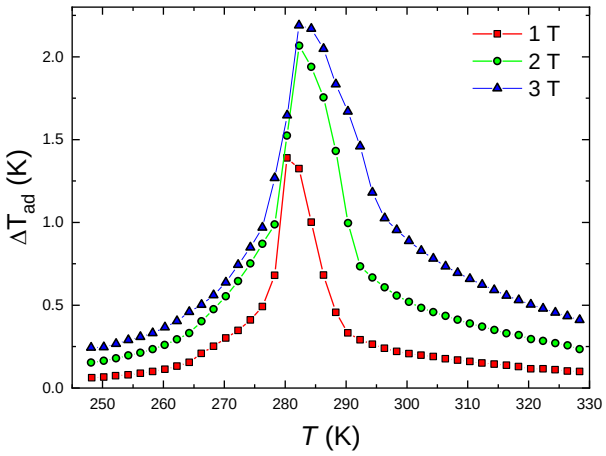

Fig. 17. Adiabatic temperature change measured directly for $Hf_{0.86}Ta_{0.14}Fe_2$.